Solar-powered tri-generation system integrating organic rankine cycle and absorption chiller for passenger trains energy supply

Energy and Built Environment xxx (xxxx) xxx

Contents lists available at ScienceDirect

Energy and Built Environment

journal homepage: http://www.keaipublishing.com/en/journals/energy-and-built-environment/

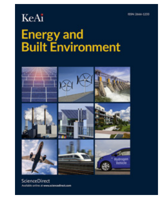

Full Length Article

Solar-powered tri-generation system integrating organic rankine cycle and absorption chiller for passenger trains energy supply

Ehsanolah Assareh[a,b], Aminhossein Jahanbin[c,*], Nima Izadyar[a,d], Mohammad Barati[e], Neha Agarwal[b]

[a] College of Sport, Health and Engineering (CoSHE), Victoria University, Melbourne VIC 3011, Australia
[b] School of Chemical Engineering, Yeungnam University, Gyeongsan 38541, South Korea
[c] Department of Architecture, Construction and Design, Polytechnic University of Bari, Bari 70126, Italy
[d] Institute for Sustainable Industries and Liveable Cities, Victoria University, Melbourne VIC 3011, Australia
[e] Department of Mechanical Engineering, Arvandan Non-profit Higher Education Institute, Khorramshahr 64199, Iran

ARTICLE INFO

Keywords:
Multi-energy system
Tri-generation
Exergoeconomic analysis
Response surface methodology (RSM)
Artificial neural network (ANN)

ABSTRACT

This study investigates the potential of leveraging solar energy to establish an integrated multi-energy production system to supply heating, cooling, and electricity for passenger trains. The proposed tri-generation system combines photovoltaic-thermal (PVT) panels, an organic Rankine cycle (ORC), an absorption chiller, and a water heater unit. The interactions between system components are examined through an exergoeconomic model developed in EES software, supported by a detailed parametric analysis. A two-step multi-objective optimization framework is implemented, integrating response surface methodology (RSM) with an artificial neural network (ANN) to improve optimization accuracy. In this framework, five decision variables and two objective functions—exergy efficiency and system cost rate—are optimized. Economic analysis reveals that the ORC unit and PVT panels incur the highest cost rates, while exergy analysis indicates that the PVT panels, absorption chillers, and evaporators experience the most significant exergy destruction. The optimal system achieves an exergy efficiency of 10.87 % and a cost rate of 1.491 $/h. The second optimization stage using the ANN method based on 100 RSM-optimized points, results in further refinement in both exergy efficiency and cost rate. A real-world case study evaluates the feasibility of implementing the proposed system on a modern passenger train along a route with high solar energy potential, analyzing its performance during a 17-hour journey across five stations and over four seasons under varying weather conditions. The findings contribute to the development of low-carbon rail transport solutions, highlighting the need for future research on energy storage, system scalability, and real-time performance optimization.

1. Introduction

With global consensus on carbon neutrality and decarbonization targets for sustainable development, the coming decade is pivotal for establishing a clear pathway to achieve net-zero emissions by 2050 and limit global warming to 1.5 °C, as outlined in the Paris Agreement [1]. In this context, the energy transition will be critical, alongside the gradual decommissioning of coal and fossil-fuel power plants and the growing adoption of renewable energy sources (RES). RES are widely recognized as the most effective and feasible solution for significantly reducing greenhouse gas emissions while meeting global energy demand sustainably [2]. As the global community faces the urgent challenge of climate change, innovative strategies and initiatives for utilizing RES across diverse sectors are essential [3]. Transportation, in particular, emerges as a key area where RES can have a transformative impact.

The transport sector is responsible for approximately 25 % of global energy consumption, including both fuel production and usage. Given this, rapidly decarbonizing transport is widely viewed as essential for addressing climate change, a position strongly endorsed by the International Energy Agency (IEA) in its Net Zero by 2050 scenario [4]. Decarbonizing transport can be achieved by replacing fossil fuels with zero-carbon fuels, which are liquid or gaseous fuels produced from RES. Another approach is to use RES-based electricity directly, either alone or alongside battery systems, or by incorporating biofuels. Compared to traditional fossil fuels and biofuels, utilizing emission-free electricity with batteries significantly lowers the well-to-wheel (WTW) energy consumption in transportation. According to Lindstad et al. [5], with these perspectives, the priorities up to 2050 should involve firstly replacing coal-fired power generation with renewable energy to nearly decarbonize the electricity grid, as this provides the highest carbon re-

Peer review under the responsibility of Southwest Jiaotong University.
* Corresponding author.
E-mail address: aminhossein.jahanbin@poliba.it (A. Jahanbin).

https://doi.org/10.1016/j.enbenv.2025.05.009
Received 14 December 2024; Received in revised form 14 May 2025; Accepted 19 May 2025
Available online xxx

Please cite this article as: E. Assareh, A. Jahanbin, N. Izadyar et al., Solar-powered tri-generation system integrating organic rankine cycle and absorption chiller for passenger train energy supply, Energy and Built Environment, https://doi.org/10.1016/j.enbenv.2025.05.009

Nomenclature

C	Specific heat [kJ/kg.K]
e_x	Specific exergy [kJ/kg]
E	Exergy rate [kW]
g	Gravity acceleration [m/s^2]
G_B	Solar irradiance [W/m^2]
h	Specific enthalpy [kJ/kg]
i	Interest rate [-]
L	Length (m)
m	Mass flow rate [kg/s]
n	Time span [hr]
P	Pressure [kPa]
Q	Thermal power [kW]
s	Specific entropy [kJ/kg.K]
T	Temperature [°C]
U	Overall heat transfer coefficient [kW/m^{2}K]
v	Velocity [m/s]
W	Power [kW]
Z	Investment cost [$]
Z	Cost rate [$/h]
Greek symbols	
η	Efficiency [-]
φ	Maintenance factor [-]
Subscripts	
0	Reference
ch	Chemical
cv	Control volume
D	Destruction
e	Exit/Out
i	In
ph	Physical
th	Thermal
w	Useful work
Abbreviation	
ANOVA	Analysis of Variance
ANN	Artificial Neural Network
CCD	Central Composite Design
Cond	Condenser
CRF	Capital Recovery Factor
DoE	Design of Experiments
Evap	Evaporator
EES	Engineering Equation Solver
GA	Genetic Algorithm
NPC	Net Present Cost
ORC	Organic Rankine Cycle
PP	Pinch Point
PVT	Photovoltaic-Thermal
RES	Renewable Energy Source
RSM	Response Surface Method

duction per unit of renewable energy. Secondly, the transport sector should be progressively electrified.

In terms of electrification of road transportation, rapid technological advancements and policy incentives have driven the global electric vehicle fleet to surpass 5.1 million units in 2018, an increase of 2 million since 2017 [6]. Electric buses represent the fastest-growing segment within this market, with approximately 380,000 electric buses operating in cities across China by the end of 2017 [7]. In Europe, 50 cities and regions have committed to the "European Clean Bus Deployment Initiative," aiming for 30 % of buses to be fossil fuel-free by 2025 [8]. However, the large-scale deployment of electric buses also presents a significant challenge to the grid due to the substantial increase in electricity demand [9].

Regarding rail transportation, it represents a significant portion of end-user consumption in the utility grid. It is anticipated that the global rail network will expand from 1.6 to 2.1 million kilometers, marking a 34 % increase from 2016 to 2050 [10]. This growth is expected to drive rail electricity demand to nearly 700 TWh by 2050, necessitating the introduction of additional power sources within the rail sector [11]. Increasing RES generation in both rail and road transportation is therefore essential for meeting this rising demand and reducing carbon emissions in the transport sector.

According to IEA [4], nearly 90 % of global electricity generation by 2050 is projected to come from RES, with solar and wind accounting for almost 70 %. However, the intermittent nature of RES-based systems, coupled with the need for diversified national grid policies, poses significant challenges to achieving a revolutionary transformation towards 100 % carbon-free energy systems [12], particularly in the transportation sector. Among various RES, solar energy is recognized as one of the most promising and widely available resources globally. Its accessibility across diverse geographic regions makes it an ideal solution for a range of applications, including public transportation systems. Despite the widespread adoption of solar energy, a gap persists between its supply and energy demand, and achieving cost-effective utilization continues to pose a major challenge [13]. In this context, RES-based co-generation and multi-energy systems that integrate hybrid solutions and advanced energy storage technologies emerge as viable solutions to address aforementioned limitations [14–16]. By optimizing the exploitation of various RES and ensuring reliable energy supply, these systems can facilitate a more resilient and sustainable energy future.

With this perspective, the literature review highlights numerous recent studies focused on hybrid solar-driven systems, each addressing different objectives. For instance, Zayed et al. [17] developed a solar air conditioning system that integrates photovoltaic (PV) panels with thermoelectric coolers, aiming to enhance thermal comfort while reducing grid-based energy use. The photovoltaic modules generate power for the solar thermoelectric air conditioning system (SPVTEAC) and charge lead-acid batteries, enabling self-sufficient operation even during nighttime hours. Lopez-Pascual et al. [18] conducted an experimental study on a geothermal cooling system to improve the efficiency of solar PV panels. The research emphasized that rising operating temperatures reduce PV panel efficiency, especially in regions with high solar irradiance and ambient temperatures. To address this, the authors proposed a compact low-enthalpy geothermal cooling system designed for commercial PV panels, aiming to mitigate the impact of heat on power output. In a techno-economic analysis, Abdolmaleki et al. [19] evaluated the feasibility of using a PV-driven hybrid system, combining metal hydride and battery storage, for the off-grid electrification of an office building in a Mediterranean climate. The study showed that the proposed hybrid system could mitigate 13.2 t CO_2/yr, with a levelized cost of electricity (LCOE) between 0.354 and 0.403 $/kWh.

In a comparative study, by introducing two solar-powered configurations based on the chemical and electrochemical energy storage systems, Esmaeilion et al. [20] explored to introduce an effective system for sustainable freshwater production in hybrid multigrid systems throughout the day. Their results showed a better performance of a chemical energy storage system by 16.48 % over an electrochemical energy storage system. Wang et al. [21] optimized the integration of solar collectors and PV panels within liquid desiccant air conditioning systems. The study demonstrated the viability of such systems by establishing their working principles and developing both physical and mathematical models for the subsystems. Energy consumption of the proposed system was systematically compared with that of conventional cooling dehumidification systems, assessing performance under different fresh air loads and heat-to-humidity load ratios. A comprehensive review on integrating thermal energy systems with solar PV panels implies that cogeneration of electricity and heat through solar systems is an efficient way to meet

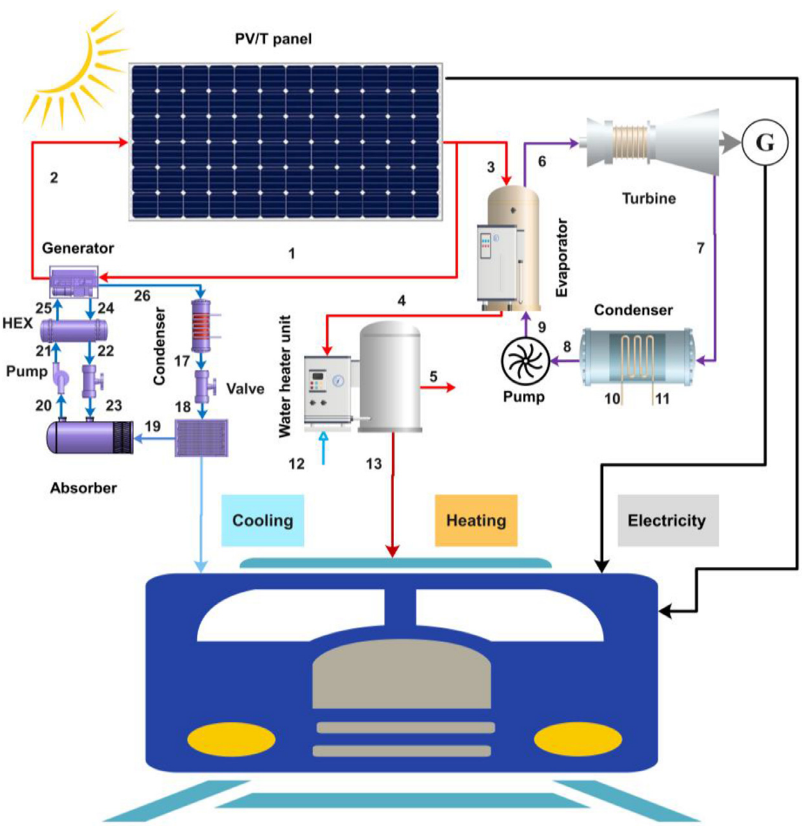

Fig. 1. Schematic diagram of the proposed integrated energy system for passenger trains.

various energy demands across sectors [22]. It emphasizes the synergistic benefits of combining thermal energy systems with PV technology for advancing sustainable energy solutions.

In the context of solar energy within the transport sector, PV generation offers a significant advantage due to its flexible installation options, making it highly suitable for integration across various transportation infrastructures. Road and rail systems, which cover extensive land surfaces, present an ideal opportunity for direct solar energy harvesting, offering the added benefit of reducing air pollution and yielding socio-economic advantages. PV systems can be easily implemented on transport infrastructure and ancillary facilities, such as station rooftops or road barriers, maximizing the use of existing spaces without increasing land consumption [11].

A notable innovation lies in the use of photovoltaic-thermal (PVT) panels on rail vehicles in regions with abundant solar resources, which efficiently convert solar energy into both electrical and thermal power to meet onboard energy needs, such as air conditioning, heating, and electrical systems. Its integration into a multi-energy production system may significantly reduce operational costs and dependence on volatile conventional energy sources, while contributing to a lower carbon footprint and environmental impacts. However, despite some exploration of solar PV in urban transportation systems [23,24], there remains a substantial research gap regarding multi-energy solar-driven systems in rail transportation, particularly in regions with high solar potential. This gap underscores the need for further investigation into the integration of solar energy in rail networks to fully capitalize on its environmental and economic benefits.

To bridge these gaps, the present study investigates the potential of an integrated multi-energy production system for passenger trains, utilizing PVT panels, an organic Rankine cycle (ORC), an absorption chiller, and a water heater. By developing a simulation model in EES software, the subtle interactions between system components are analyzed. A bi-level multi-objective optimization framework, combining response surface methodology (RSM) and artificial neural network (ANN) techniques, optimizes five decision variables and two conflicting objectives—exergy efficiency and system cost. An economic assessment of the system is conducted to evaluate the financial viability and cost-effectiveness of the proposed energy solution. A real-world case study is conducted to assess the feasibility of implementing the proposed system on a modern passenger train, evaluating its performance across different weather conditions at five stations over the course of a 17-hour journey through all four seasons. The findings of this study are expected to contribute to the advancement of renewable energy applications in the rail transportation sector, paving the way for more sustainable practices in public transit systems.

2. System description

The proposed system in this study explores the potential of harnessing solar energy to create an integrated multi-energy production system for passenger trains. It is specifically engineered to capture solar energy through the integration of PVT panels and is designed to generate both electricity and thermal energy to meet the energy demands of passenger trains. Fig. 1 illustrates the schematic design of the proposed system.

The system consists of several key components: a PVT panel subsystem, an ORC, a water heater, and an absorption chiller unit. The primary outputs of this integrated system are electricity, cooling, and heated water—all of which are essential for the efficient operation of passenger trains.

In this configuration, the thermal energy required by the ORC is supplied by the PVT panels, which transfer heat to the ORC working fluid via an evaporator. A key advantage of integrating PVT panels lies in their dual functionality, as they simultaneously generate both electricity and thermal energy. Upon heat transfer to the evaporator, the working fluid undergoes phase change into vapor, driving the turbine to produce mechanical power, which is subsequently converted into electricity. The electrical output from the turbine is then integrated with the power generated by the PVT panels to supply a stable and reliable energy source

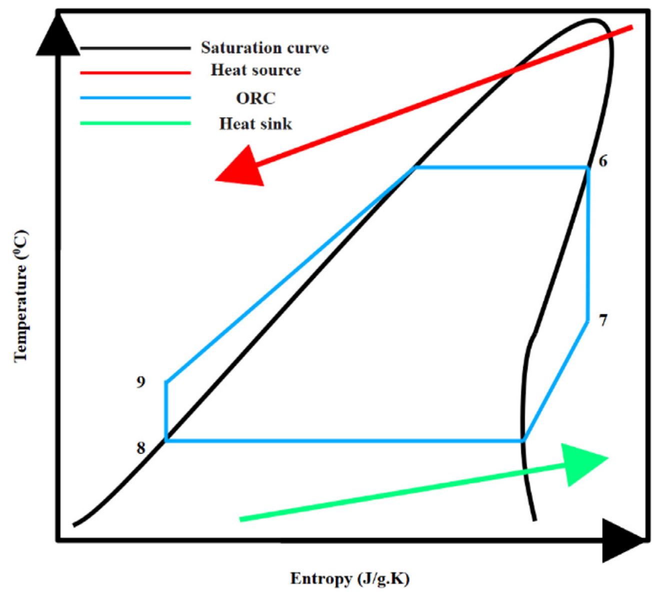

Fig. 2. Temperature-Entropy (T-S) diagram of the Rankine cycle within the cogeneration system.

for the passenger train. Fig. 2 presents a temperature-entropy (T-S) diagram to visualize the thermodynamic behavior of a Rankine cycle within this cogeneration system. The plot systematically tracks state-specific changes in temperature (*T*) and entropy (*s*) across critical cycle components, including the turbine, condenser, pump, and evaporator.

Furthermore, the waste heat from the ORC evaporator is utilized for water heating, enhancing overall system efficiency. An absorption chiller, comprising a condenser, evaporator, absorber, generator, and heat exchanger, utilizes the thermal energy extracted from the hot water produced by the PVT panels to deliver cooling, thereby further optimizing energy utilization within the system.

This approach is expected to enhance the system's energy efficiency while reducing reliance on conventional fossil fuels, contributing to a lower environmental impact. The proposed solar energy system represents a step forward in integrating renewable technologies into transportation. By harnessing solar energy, it offers a sustainable and environmentally conscious solution for powering passenger trains, with the potential for broader applicability across the transportation sector.

3. Methodology

To examine the techno-economic feasibility and performance of the proposed cogeneration system, a structured methodology is implemented. The adopted procedural framework, summarized in Fig. 3, presents a comprehensive and systematic approach to system modeling, optimization, and performance analysis. By leveraging the capacity of EES software and multi-objective optimization techniques, this research aims to develop an efficient and cost-effective solution to meet the energy demands of passenger trains, while evaluating system performance on an actual train route, ensuring adaptability and resilience in real-world operations.

The first step involves modeling the system using EES software, which can solve complex, coupled nonlinear algebraic and differential equations. EES offers precise thermodynamic and transport property functions for various fluids, ensuring accurate simulation of the system's components. To enhance system performance, a bi-level multi-objective optimization framework is developed, combining RSM and ANN. This optimization focuses on two critical objectives: maximizing exergy efficiency to boost the system's technical performance and minimizing the system's cost rate to improve its economic feasibility.

A real-world case study evaluates the feasibility of implementing the proposed system on a passenger train in Iran, assessing its performance under variable climatic conditions at five stations across four seasons. The spatial analysis, integrated into the methodology, evaluates system performance as the train travels through key cities such as Ahvaz, Khorramabad, Arak, Qom, and Tehran. By incorporating these geographical variables, the study examines how the system adapts to changing weather and environmental conditions. The weather data, sourced from

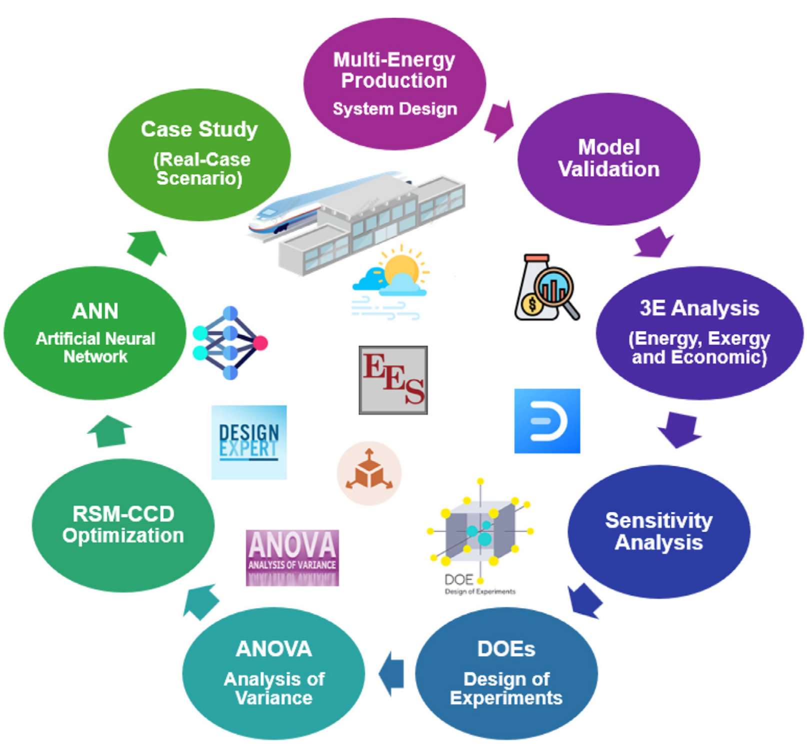

Fig. 3. Schematic representation of the procedural steps followed in this study.

Table 1
The input data used for the preliminary analysis of the proposed system.

Data	Value
pp_{Evap}	5 (°C)
pp_{Cond}	5 (°C)
T_6	95 (°C)
T_8	40 (°C)
m_{air}	2 (kg/s)
η_{turbin}	0.8 (%)
η_{pump}	0.8 (%)

Meteonorm software, provides a robust foundation for evaluating system behavior across various climates. The following sections provide further details on the methods adopted for techno-economic analysis and optimization algorithms.

3.1. Exergoeconomic analysis

The following assumptions are made to simplify the problem [25,26]:

- The process is in a steady-state condition.
- The turbine and the pump are isentropic.
- The pressure drop in pipelines is insignificant.
- Condenser output is saturated liquid.
- Evaporator output is saturated steam.
- Changes in kinetic and potential energy are insignificant.

The analysis begins with the conservation of mass, defined in Eq. (1), where mass flow rates remain constant across system components:

$$\sum_k \dot{m}_i - \sum_k \dot{m}_e = \frac{dm_{cv}}{dt} \tag{1}$$

The first law of thermodynamics ensures energy conservation, given by:

$$\dot{Q} - \dot{W} + \sum_i \dot{m}_i\left(h_i + \frac{v_i^2}{2} + gZ_i\right) - \sum_e \dot{m}_e\left(h_e + \frac{v_e^2}{2} + gZ_e\right) = \frac{dE_{cv}}{dt} \tag{2}$$

Using the second law of thermodynamics, the exergy balance is as follows:

$$\dot{E}x_Q + \sum_i \dot{m}_i(ex_i) = \sum_e \dot{m}_e(ex_e) + \dot{E}x_w + \dot{E}x_D \tag{3}$$

Other components are calculated using the following relationships:

$$\dot{E}x_Q = \left(1 - \frac{T_0}{T_i}\right)\dot{Q}_i \tag{4}$$

$$\dot{E}x_w = \dot{W} \tag{5}$$

$$ex = ex_{ph} + ex_{ch} \tag{6}$$

The amount of physical exergy is obtained from Eq. (7):

$$\dot{E}x_{ph} = \sum_i \dot{m}_i\left(\left(h_i - h_0\right) - T_0\left(s_i - s_0\right)\right) \tag{7}$$

Table 1 reports the input data used for the preliminary analysis of the proposed system.

Using Eq. (8), the amount of useful energy produced in the PVT panel is obtained:

$$\dot{Q}_{PVT} = \left[\frac{\dot{m}_{air}C_{air}}{U_l}.\left(h_{p2g}G_Bf_Z\right) - U_l\left(T_{air,in} - T_O\right)\right].\left(1 - exp\left(\frac{-bU_lL}{\dot{m}_{air}C_{air}}\right)\right) \tag{8}$$

Table 2
Correlations representing the energy balance of different subsystems within the multi-energy system.

Components	Equation
Turbine	$\dot{W}_{Turbine} = \dot{m}_6 \times (h_6 - h_7)$
Pump	$\dot{W}_{Pump} = \dot{m}_8 \times (h_9 - h_8)$
Evaporator	$Q_{Evaporator} = \dot{m}_9 \times (h_6 - h_9)$
Water Heater	$Q_{WaterHeater} = \dot{m}_{12} \times (h_{13} - h_{12})$

Table 3
Equations related to the cost of each system's component.

Components	Equation
Panel PVT	$Z_{PVT} = 310 \times L \times b$
Turbine	$Z_{Turbine} = 4750 \times ((\dot{W}_{turbine}^{0.75}) + 60 \times (\dot{W}_{turbine}^{0.95}))$
Pump	$Z_{Pump} = 3500 \times (\dot{W}_{Pump}^{0.41})$
Condenser	$Z_{Condenser} = 150 \times (A_{Condenser}0.8)$
Evaporator	$Z_{Evaporator} = 276 \times (A_{Evapl}{}^{0.88})$
Water Heater	$Z_{WaterHeater} = 0.3 \times \dot{m}_{13}$
Absorption chiller	$Z_{Chiller} = Q_{Cooling}{}^{0.67}$

where Q_{PV} is the useful thermal energy output, m_{air} is the air mass flow rate, C_{air} is the specific heat of air, U_l is the overall heat transfer coefficient, $h_{p2g}$is the secondary heat transfer coefficient, G_B is the beam solar radiation, b is a collector width parameter, and L is the panel length.

The output power of the PVT panel is obtained from Eq. (9):

$$\dot{W}_{PVT} = \eta_{PV}.T_{cell}.\tau.G_b.A \tag{9}$$

where W_{PVT} is the electrical power generated by the PV system, η_{PV} is the PV module's conversion efficiency, τ is the transmissivity of the glass cover, and A ($b \times L$) is the surface area of the collector.

The thermal efficiency of the solar panel is also calculated by:

$$\eta_{th} = \dot{Q}_{PVT}/G_B.b.L \tag{10}$$

Regarding the energy balance of subsystems in the multi-energy system, Table 2 presents the corresponding correlations used in this research.

The value of the total power of the system is obtained by:

$$\dot{W}_{net} = \dot{W}_{Turbin} + \dot{W}_{PVT} - \dot{W}_{Pump} \tag{11}$$

Furthermore, the exergy efficiency of the system is calculated using Eq. (12)

$$\eta_{ex} = \frac{(\dot{W}_{net} + Q_{th}) \times 100}{Ex_{sun}} \tag{12}$$

The cost rate of each component is given by [27]:

$$\dot{Z} = \frac{Z \times CRF \times \varphi}{t} \tag{13}$$

The capital recovery factor (CRF) is obtained through the following equation [27]:

$$CRF = \frac{i(1+i)^n}{(1+i)^n - 1} \tag{14}$$

Table 3 presents the equations related to the cost of each component.

The total cost of the system is obtained from the total cost of the system components and is calculated as follows:

$$Z_{total} = Z_{PVT} + Z_{Turbine} + Z_{Condenser} + Z_{Evaporator} + Z_{Pump} + Z_{Chiller} + Z_{WaterHeater} \tag{15}$$

3.2. Hybrid two-step optimization (RSM-ANN)

In this research, a hybrid optimization approach combining RSM and ANN is employed to analyze the output data from the multi-energy production system. The optimization process is carried out in two stages:

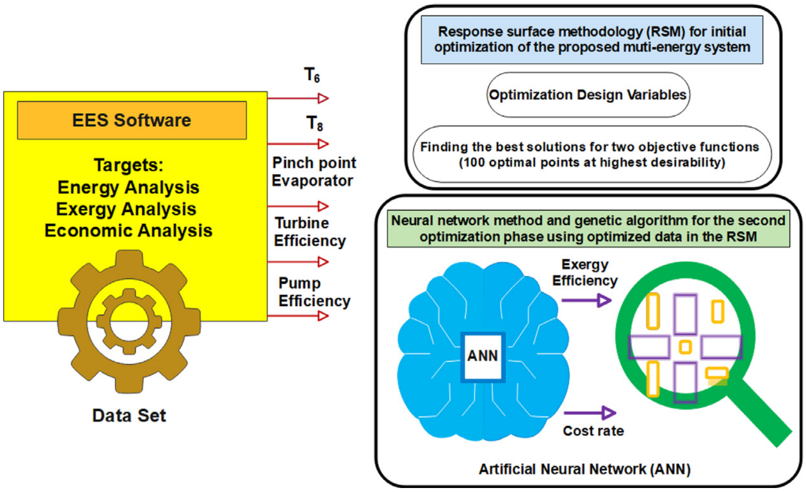

Fig. 4. Description of the two-step optimization process developed in this study.

First, the data is optimized using the RSM method. In the second stage, the optimized results from RSM are used to train an ANN model. Finally, the coefficients of the ANN-generated mathematical function are further optimized using a multi-objective optimization method.

Multi-objective optimization involves the simultaneous optimization of multiple, often conflicting objectives. In this case, the optimized coefficients are used to minimize or maximize specific objective functions. The outcome of this multi-objective optimization is the identification of optimal trade-offs between competing objectives, providing valuable insights into the system's overall performance. The optimization process targets two key objectives: enhancing exergy efficiency to improve the system's technical performance and reducing the cost rate to increase its economic viability. Fig. 4 illustrates the integration of RSM, ANN, and multi-objective optimization techniques in the optimization process.

The hybrid approach leverages the strengths of each method, delivering a comprehensive framework for optimizing the multi-energy production system. By combining the data-driven capabilities of RSM and ANN with the capacity to address multiple objectives, this methodology provides a robust and reliable solution to guide the design and operation of the system effectively. In the following, details of the methodology adopted in each step are discussed.

3.2.1. Response surface methodology (RSM)

In this study, RSM has been utilized for the initial optimization of the techno-economic performance of the multi-energy system. This technique is a comprehensive set of statistical and mathematical methods designed to model and analyze problems where a response of interest is influenced by multiple variables [28]. By establishing a functional relationship between one or more response variables (outputs) and multiple independent variables (inputs), the effect of each parameter and its interactions can be quantitatively assessed. At the same time, the optimal combination of parameter levels can be identified based on specific response criteria, a process known as RSM-based optimization [29].

The core aim of RSM is to optimize this response by establishing the precise relationship between controllable input parameters and the resulting output. The optimization process using RSM involves crucial steps such as the design of experiments (DOEs), systematic data collection, and analysis of variance (ANOVA) to ensure accuracy and reliability. By applying RSM, a refined set of optimized data points can be generated, which serves as the foundation for the subsequent neural network analysis [30]. This method is commonly employed in engineering and energy research studies [31–33] because it effectively models and analyzes nonlinear relationships between multiple variables and outcomes—something that traditional optimization methods often struggle to address. The flowchart in Fig. 5 illustrates the different steps applied in the RSM approach.

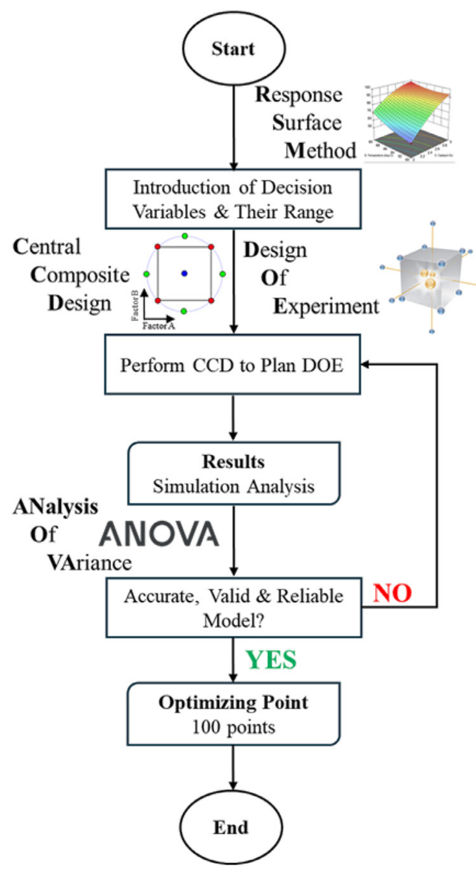

Fig. 5. A flowchart representing the employed RSM approach.

3.2.2. Artificial neural network (ANN)

An artificial neural network (ANN) represents an advanced machine learning model inspired by the neural architecture of biological organisms, particularly the human brain. Comprising interconnected artificial neurons, an ANN processes input signals through multiple layers—typically including input, hidden, and output layers—where each neuron applies a non-linear activation function to its input data. The strength of connections between neurons, represented by adjustable weights, evolves during training to optimize performance. An ANN excels at identifying patterns within complex, often nonlinear datasets, making it indispensable in applications such as predictive modeling,

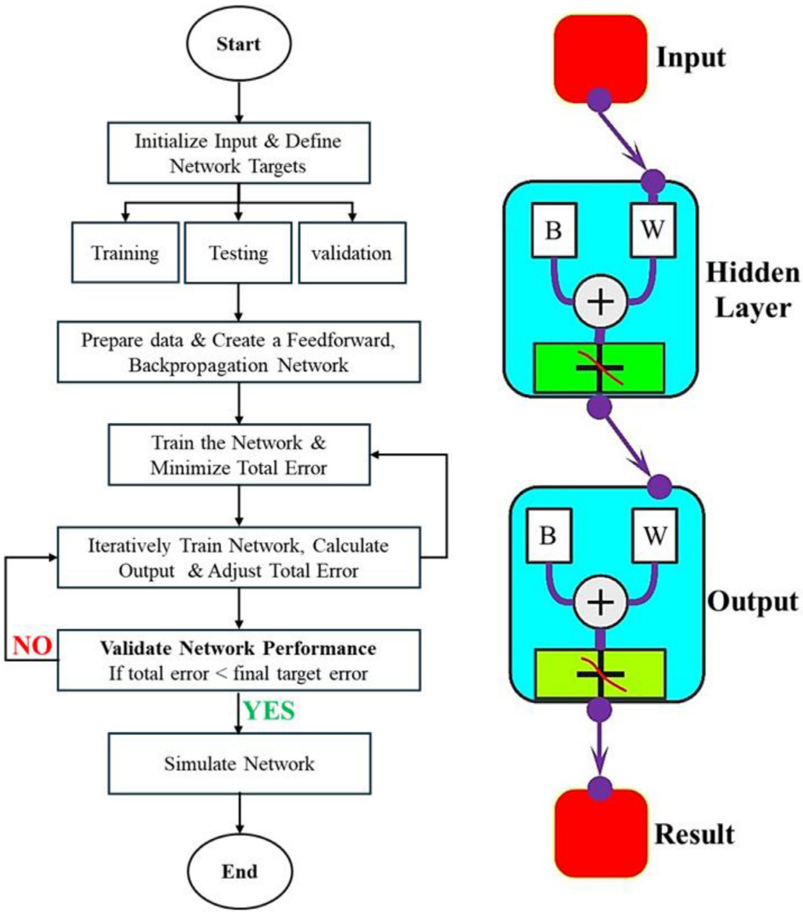

Fig. 6. The flowchart and structure of the applied artificial neural network method.

image processing, speech recognition, and natural language processing. Its ability to learn from experience, along with advancements in computational power, continues to expand its role in addressing increasingly intricate problems within artificial intelligence (AI) systems [34–36].

In this study, the ANN models the behavior of the system using data optimized through the RSM approach. The ANN trains to identify underlying patterns and dependencies in the data, enabling the derivation of a mathematical function that accurately represents system behavior. Fig. 6 illustrates the flowchart and structure of the ANN method applied in this research. By leveraging the ANN's learning capabilities, the optimal coefficients for the mathematical function are extracted, improving the precision of the model's predictions and demonstrating the network's versatility in handling complex data relationships.

4. Results and discussion

4.1. Model validation

To ensure the accuracy of the developed cogeneration system model in EES, a validation process has been conducted prior to analyzing the proposed system. The results of this research have been compared with the findings from the study by Amiri Rad et al. [37]. In their work, waste heat from industrial complexes, with temperatures ranging from 120 to 300 °C, was used to generate power through an ORC using various working fluids. They performed simultaneous optimization of the working fluid and boiler pressure for different heat source temperatures in the ORC.

For validation, similar inputs to the Amiri Rad et al. [37] study have been assumed, including the working fluid (R152a), heat source temperature, mass flow rate, and turbine inlet pressure. In the model validation, the thermophysical properties of R152a were obtained from the EES database, ensuring accurate fluid property estimations. Key outputs, such as turbine power, system output power, and thermal efficiency, have been then examined. A comparison of the results revealed an acceptable deviation, with a maximum error of 3.04 %, confirming the accuracy of the ORC model established in this research. The corresponding model validation data are reported in Table 4.

4.2. Parametric study

The inlet temperature of ORC turbines is a key factor affecting both system performance and economic. The ORC turbine inlet temperature range (80–120 °C) corresponds to the heat supply characteristics of the integrated PVT system. The working fluids, R152a for ORC and H_2O-LiBr for the absorption chiller, were selected based on thermodynamic suitability and environmental impact. As the inlet temperature rises, the working fluid's enthalpy increases, leading to greater turbine power output and enhanced overall system capacity. Fig. 7 illustrates this relationship, showing a clear increase in production power as the inlet temperature climbs from 80 °C to 120 °C. This rise in power generation also improves exergy efficiency and cost rate, both of which are tied to production power. Additionally, higher turbine inlet temperatures enhance the system's heating output, reflecting improved thermal performance. However, the cooling output remains stable despite temperature changes, as the absorption chiller operates independently of the turbine temperature. The observed trends in output power and exergy efficiency result from the trade-off between enthalpy drop and system irreversibility, while the limited variation in exergy efficiency reflects the system's inherent thermal stability at low-grade temperatures. The findings underscore the importance of optimizing ORC turbine inlet temperatures to maximize energy production and system efficiency.

Table 4
Model validation data.

Parameter	Unit	Present model	Amiri rad et al. [37]	Error (%)
Working fluid	-	R152a	R152a	-
Temperature heat source	˚C	150	150	-
Mass flow heat source	kg/s	15	15	-
Inlet pressure turbine	bar	27.3	27.3	-
Turbine power	kW	118.1	121.8	3.04
Output power of the system	kW	107.2	105.8	1.32
Thermal efficiency	%	7.90	7.74	1.98

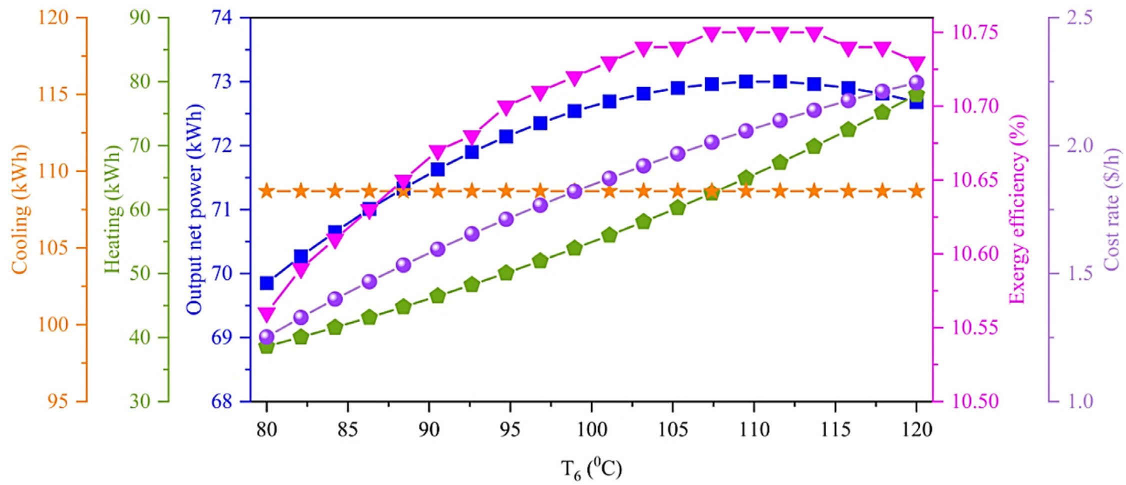

Fig. 7. Effects of variations in the turbine inlet temperature on the system performance.

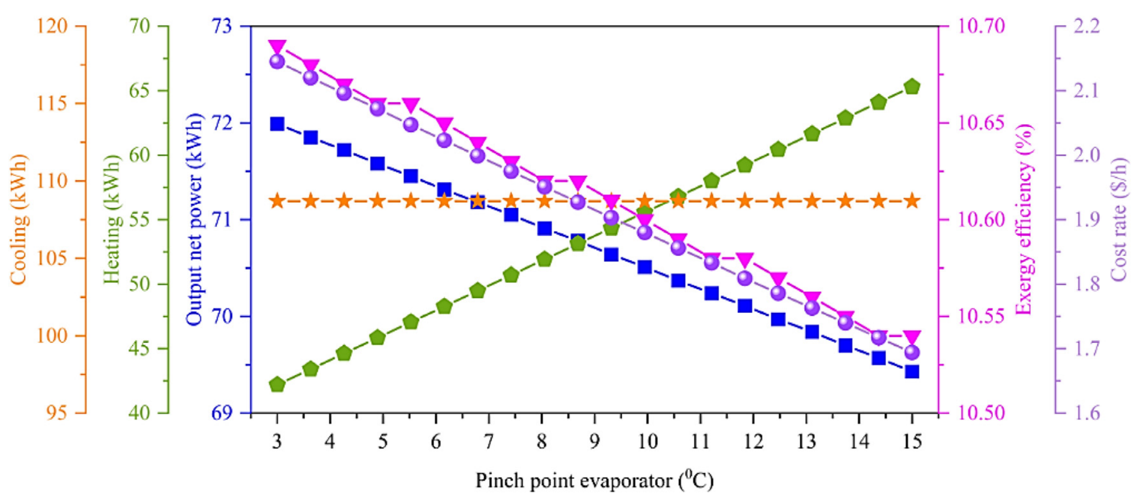

Fig. 8. Effects of variations in the evaporator pinch point temperature on the system performance.

As shown in Fig. 8, the evaporator pinch point temperature varies from 3 ˚C to 15 ˚C, while the ORC turbine inlet temperature, turbine efficiency, and pump efficiency are maintained at 110 ˚C, 88 %, and 86 %, respectively. Increasing the pinch point temperature from 3 ˚C to 15 ˚C results in a steady decline in net power output, dropping from about 72 kWh to 69.5 kWh—a 3.5 % decrease. This reduction is attributed to the diminished thermal gradient between the working fluid and the heat source, which lowers heat transfer efficiency within the ORC. Consequently, the system's exergy efficiency also declines, from 10.68 % at 3 ˚C to 10.53 % at 15 ˚C, indicating a reduction in overall thermodynamic performance. The cost rate exhibits a downward trend as well, decreasing from 2.15 $/h to 1.70 $/h, namely a 20.9 % reduction. Although a lower cost rate reflects reduced energy input requirements, it occurs at the expense of power generation efficiency, which is crucial for maintaining consistent system performance. Conversely, the heating output shows a 59.5 % increase, rising from 42 kWh at 3 ˚C to 67 kWh at 15 ˚C.

The results presented in Fig. 9 indicate a significant correlation between turbine efficiency and the overall power output of the system. Increasing turbine efficiency from 70 % to 95 % leads to a steady rise in net power output from 68.4 kWh to 73.6 kWh (7.6 % increase) due to reduced internal energy losses, allowing more energy to be effectively converted into mechanical power. Similarly, exergy efficiency increases highlighting the thermodynamic benefits of improved turbine performance. However, the cost rate shows about an 8.0 % increase, indicating that while higher turbine efficiency enhances power generation, it also raises system investment and operational costs. Moreover, despite these variations in power and efficiency, changes in heating and cool-

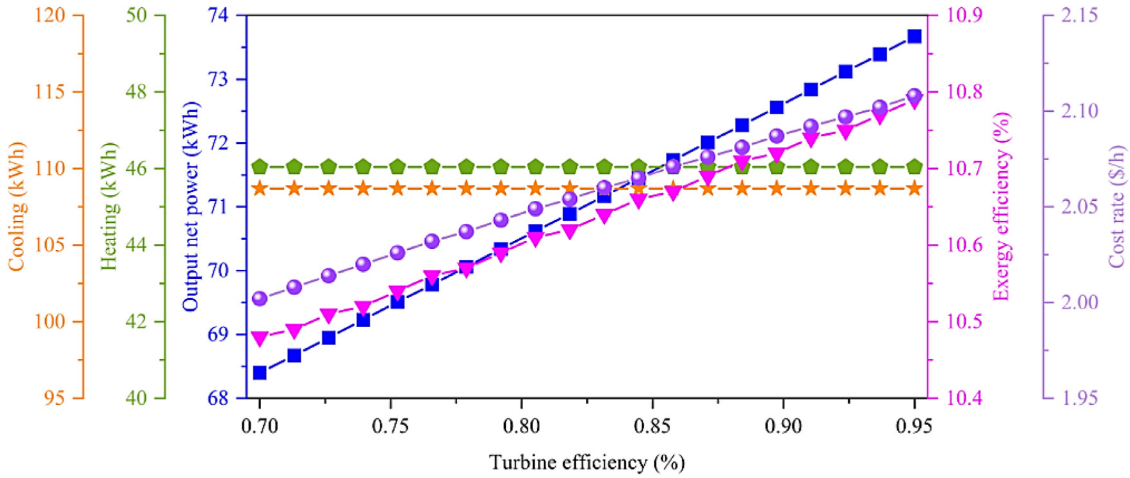

Fig. 9. Effects of variations in turbine efficiency on the system performance.

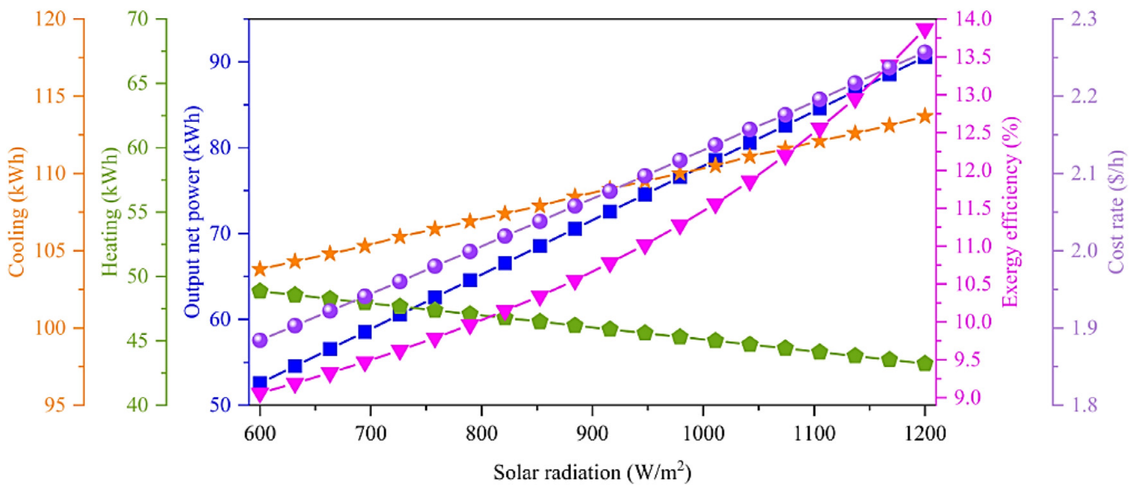

Fig. 10. Effects of variations in the solar radiation intensity on the system performance.

ing remain marginal, demonstrating their independence from turbine efficiency fluctuations.

The results depicted in Fig. 10 illustrate the direct influence of solar radiation intensity on the performance of the multi-energy production system. Increasing solar radiation intensity from 600 to 1200 W/m^2 leads to a 73.1 % increase in net power output, from 52 kWh to 90 kWh. This enhancement results from higher thermal energy absorption by the PVT panels, which increases the working fluid's temperature and flow rate, thereby improving mechanical power generation. Exergy efficiency follows a similar trend, rising from 9.0 % to 13.8 %. However, the cost rate increases from 1.90 $/h to 2.25 $/h (18.4 % increase), indicating that while higher solar radiation enhances system performance, it also raises investment and operational costs due to increased energy processing demands.

Notably, unlike the heating capacity, the cooling production increases steadily with solar radiation as the absorption chiller benefits from greater thermal availability, supporting enhanced cooling output. As solar radiation increases, a larger share of the available energy is allocated to electricity generation and cooling, thereby reducing the residual heat available for direct heating. This results in a gradual decline in heating output, as a greater portion of thermal energy is converted into mechanical power and cooling capacity instead of being retained for heating purposes.

Fig. 11 shows the impact of increasing the pump inlet temperature from 20 ˚C to 40 ˚C on the multi-energy production system. As the inlet temperature rises, the system's production power decreases. This reduction occurs due to lower working fluid density and viscosity at higher temperatures, which affects pump flow rates and pressure stability, ultimately reducing thermodynamic efficiency. As a result, exergy efficiency decreases from 11.0 % to 10.55 %, reinforcing the adverse effect of elevated inlet temperatures on energy conversion efficiency. The cost rate also declines from 2.3 $/h to 1.95 $/h (15.2 % reduction), reflecting the lower operational energy demands at reduced power output levels. However, the heating output shows a 57.7 % rise as the higher inlet temperature enhances thermal energy transfer to the evaporator, boosting the heating system's performance.

4.3. Hybrid optimization results

The multi-objective optimization process begins by identifying 100 optimal solutions using the RSM approach, which pinpoints the most favorable values for both objective functions and optimization variables. In this study, five influential design parameters are chosen as the optimization variables. The design variables include the turbine and pump inlet temperatures, pump and turbine efficiencies, and pinpoint evaporator temperature. These parameters were selected due to their significant influence on system performance, exergy destruction, and operational costs. Specifically, turbine efficiency and pump efficiency play a crucial role in governing energy conversion, fluid circulation, and electricity generation, directly impacting the system's thermodynamic and

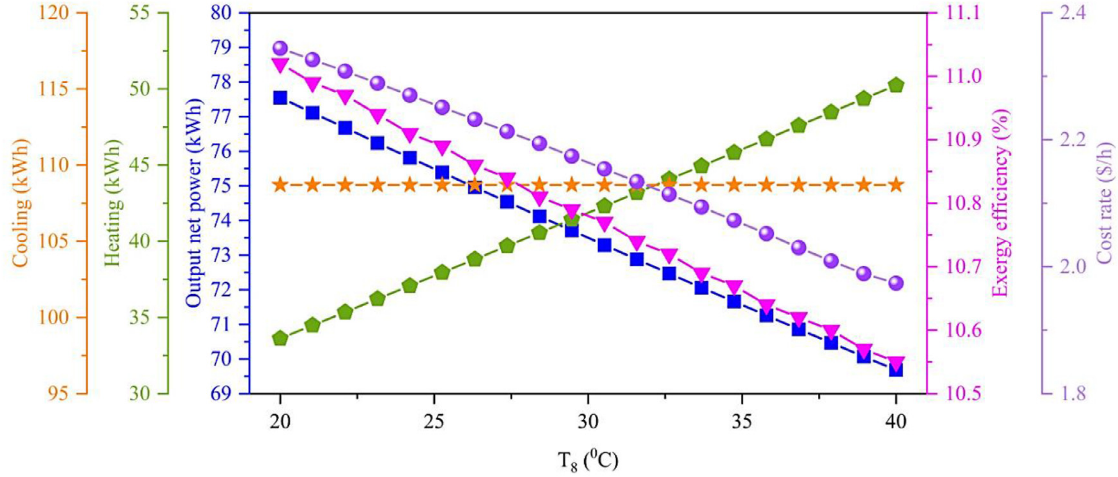

Fig. 11. Effects of variations in the pump inlet temperature on the system performance.

Table 5
The optimization design variables in RSM-CCD and their lower and upper limits.

Design Variable	Lower Limit	Upper Limit
T_6 (°C)	80	120
T_8 (°C)	20	40
Pump efficiency (-)	0.7	0.95
Turbine efficiency (-)	0.7	0.95
Pinch point evaporator (°C)	3	15

Table 6
The optimal value of the design variables and objective functions obtained by RSM-CCD.

Parameter	Optimum point
Turbine efficiency (-)	0.881
Pump efficiency (-)	0.867
Pinch point evaporator (°C)	10.239
T_6 (°C)	108.944
T_8 (°C)	25.528
Exergy efficiency (%)	10.873
Cost rate (%)	1.491
Desirability	0.804

Table 7
The optimal range of objective functions.

Name	Goal	Lower Limit	Upper Limit
Exergy efficiency (%)	Maximize	10.50	10.96
Cost rate (%)	Minimize	1.284	2.302

economic outcomes. The objective functions are the exergy efficiency and the system cost rate. The optimization aims to maximize exergy efficiency and minimize system cost, ensuring an optimal balance between performance improvement and economic feasibility. By varying these parameters within their predefined ranges, as shown in Table 5, the optimization process effectively explores the design space, identifying configurations that enhance energy efficiency while reducing costs.

The results of this process are presented in Table 6, which showcases the outcomes of 100 optimal points identified using the RSM approach in the Design Expert software framework. By prioritizing solutions with higher desirability scores, the optimization process successfully identifies the optimal values for the design variables, effectively balancing the competing objectives of maximizing exergy efficiency and minimizing system cost. Furthermore, the optimal range of objective functions, with the highest desirability score of 0.804, is detailed in Table 7, marking it as the most favorable range within the 100 optimal points evaluated. The narrow exergy efficiency range (10.50 %–10.96 %) results from the limited impact of decision variables on system irreversibility within the constrained low-grade temperature range, where improvements remain marginal due to thermodynamic constraints.

Fig. 12 illustrates a contour plot that captures the variations in exergy efficiency triggered by changes in several critical design parameters. The predicted optimal exergy efficiency is 10.873 %, achieved through a well-balanced combination of design parameters. Higher turbine efficiency improves exergy efficiency from 10.6 % to 11.1 %, demonstrating the thermodynamic advantage of reducing irreversibility in energy conversion. Similarly, increasing T_6 from 80 °C to 120 °C enhances exergy efficiency due to higher available energy for conversion, peaking at 10.9 %–11.0 % before stabilizing. However, raising the evaporator pinch point temperature negatively affects exergy efficiency, with values declining as it increases from 3 °C to 15 °C, emphasizing the trade-off between improved heating performance and reduced energy conversion efficiency. On the other hand, higher pump inlet temperatures (T_8) result in lower exergy efficiency, decreasing from 10.9 % at 25 °C to 10.6 % at 40 °C, likely due to density reduction and energy losses in fluid handling.

In Fig. 13, the contour plot focuses on the cost rate of the system, with the primary goal being to minimize this objective function. Similar to the results for exergy efficiency, the four key parameters emerge as the most influential in determining the cost rate. The analysis targets an optimal cost rate of 1.491 $/h, reflecting a balanced approach between performance and cost. Higher turbine efficiency (with an increase in pinch point) reduces the cost rate, decreasing from 1.8 $/h at 70 % efficiency to 1.2 $/h at 95 % efficiency (33 % reduction), as more energy is converted into useful work, lowering operational expenses. Similarly, for a given turbine efficiency, increasing T_6 from 80 °C to 120 °C decreases the cost rate from 2.2 $/h to 1.2 $/h (45 % reduction) due to enhanced system efficiency and reduced wasted energy. Unlike exergy efficiency, which exhibits complex nonlinear responses to design variables, the cost rate follows a more predictable quasi-linear trend, particularly to turbine efficiency and T_6. These results confirm that strategic parameter selection is crucial for minimizing costs while maintaining energy efficiency, ensuring an economically viable and high-performance multi-energy system.

The second stage of the hybrid optimization process focuses on refining the precision of initial results through re-optimization using the ANN method. Building on the optimal solutions obtained from the RSM,

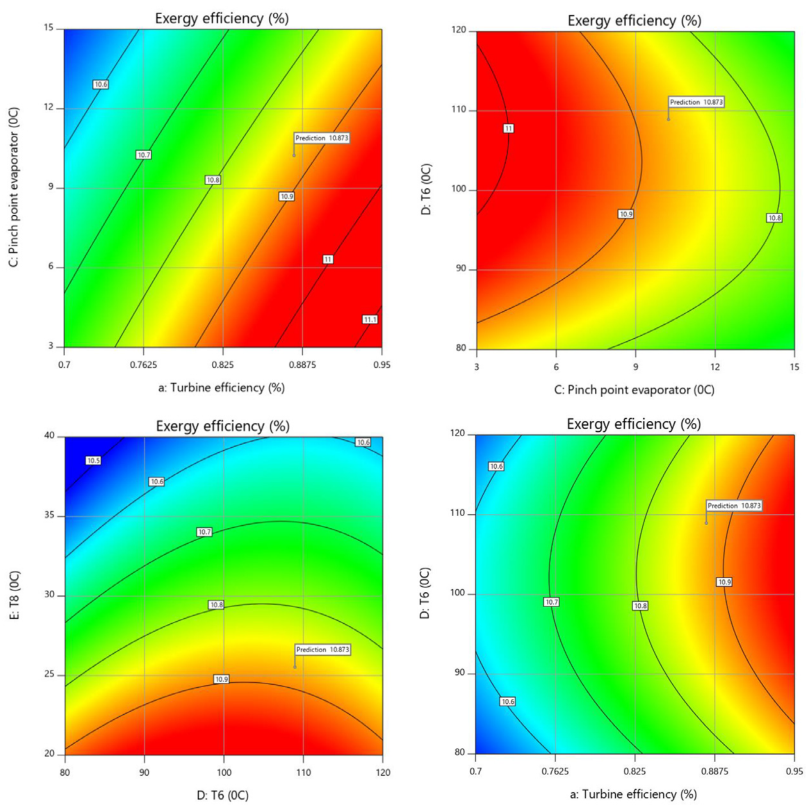

Fig. 12. Alterations in the exergy efficiency triggered by changes in the design variables.

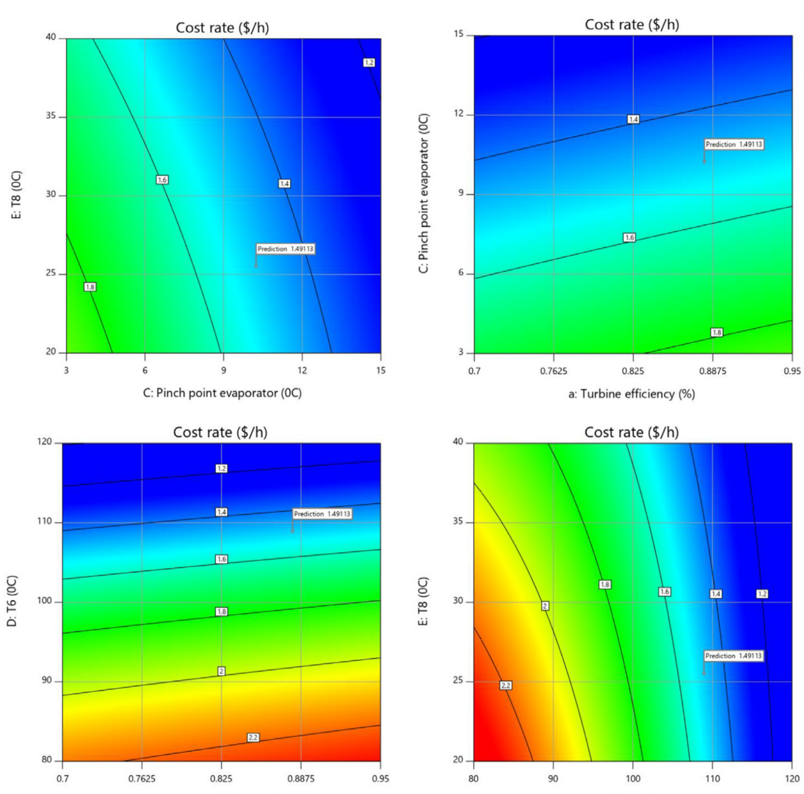

Fig. 13. Variations in the cost rate resulting from changes in the design variables.

Table 8
Optimum value of decision-making variables and objective functions.

Parameter	Mean	Minimum	Maximum
Pump efficiency (-)	0.838	0.769	0.881
Turbine efficiency (-)	0.879	0.863	0.881
Pinch point evaporator (°C)	9.606	6.317	11.683
T_6 (°C)	108.909	107.909	108.944
T_8 (°C)	25.609	25.528	26.998
Exergy efficiency (%)	10.882	10.813	10.953
Cost rate ($/h)	1.520	1.416	1.668

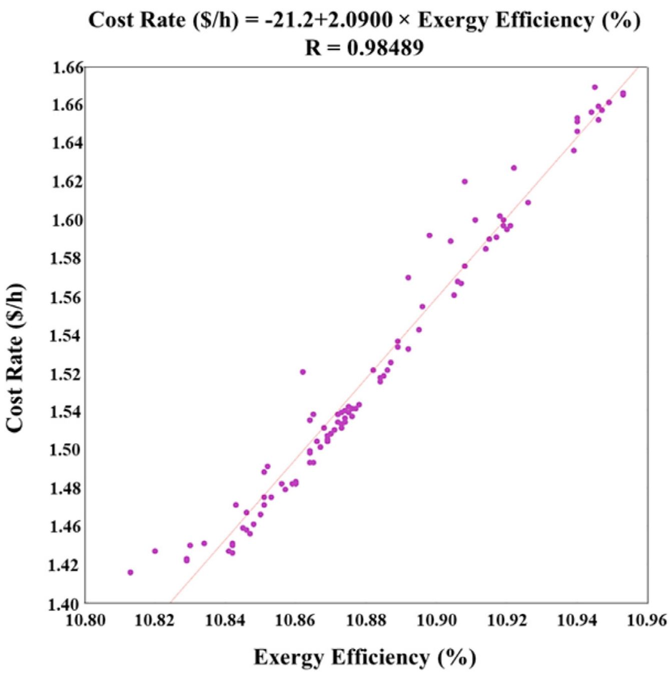

Fig. 14. Pareto front plot for objective functions in multi-objective optimization.

the ANN method is employed to further enhance accuracy. The data extracted from system modeling serves as input for the neural network, which is then optimized using meta-heuristic algorithms to achieve the best trade-offs between design variables and objective functions, namely the exergy efficiency and system cost rate. This hybrid approach leverages the strengths of both methods, with RSM facilitating initial exploration and ANNs providing a more refined model.

The final optimal values of the decision variables and objective functions are presented in Table 8, which marks the culmination of the hybrid optimization process. The table provides a detailed summary of the minimum, maximum, and mean optimal values for both the design variables and the objective functions, offering a comprehensive overview of the optimization results. It shows that the exergy efficiency is optimized to a mean value of 10.882 %, exceeding the lower bound of 10.813 %, while the cost rate varies between 1.416 $/h and 1.668/ $/h, with a mean value of 1.520 $/h.

Fig. 14 demonstrates the trade-off relationship between exergy efficiency and system cost rate, forming a Pareto front that delineates the optimal balance between performance and economic feasibility. The strong linear correlation ($R^2 = 0.985$) indicates that increasing exergy efficiency directly leads to higher costs, as reflected in the cost rate equation based on exergy efficiency (%). The cost rate rises from 1.42 $/h at 10.82 % exergy efficiency to 1.66 $/h at 10.96 %, representing a 16.9 % cost increase for a 1.3 % efficiency gain, underscoring the diminishing returns of efficiency improvements. This front portrays the set of solutions in which improvements in one objective, such as maximizing exergy efficiency, necessitate trade-offs in the other, such as minimizing system cost. Identifying Pareto optimal solutions establishes a solid foundation for effectively balancing system performance and economic considerations.

Fig. 15 presents histograms showing the frequency distribution of the optimized objective functions, namely the exergy efficiency and cost rate, alongside the expected normal distribution curve. The horizontal axis represents the values of the objective functions, while the vertical axis displays the frequency. For exergy efficiency, the data reveals a higher frequency of values within the 10.84 % to 10.92 % range, indicating this as the most frequent outcome of the optimization process. Similarly, the cost rate shows a high frequency in the range of 1.40 $/h to 1.60 $/h.

To further assess the accuracy of the optimization predictions, Fig. 16 provides a comparison of the raw residuals for the exergy efficiency and cost rate against the optimized ranges reported in Table 8. The residuals, which represent the difference between predicted and actual values, are primarily clustered around zero. This indicates a high level of precision in the optimization model's predictions, as the minimal deviations confirm the reliability of the predicted outcomes. Additionally, the absence of significant outliers confirms that the model effectively captures the relationship between design parameters and objective functions.

4.4. *Exergy and economic analysis*

Fig. 17 presents the exergy analysis of the proposed multi-energy production system under optimal conditions. The system begins with a total solar input exergy rate of 1948 kWh, directed to the solar panel. From this input, 54 kWh of useful energy is generated, while 1633 kWh is lost due to inefficiency. Following the solar panel, the evaporator receives 110 kWh of exergy, with 10 kWh lost during transfer. The turbine extracts 38 kWh from the evaporator, converting 22 kWh into electricity, while 2 kWh is lost to the condenser. The water heater receives 72 kWh of exergy, with a minimal loss of 4 kWh, producing 68 kWh of heating energy. The absorption chiller, receiving 151 kWh, loses 43 kWh but generates 108 kWh of cooling energy. Notably, the pump exhibits the lowest exergy loss, indicating its higher efficiency compared to other system components. The analysis identifies the solar panel, absorption chiller, and evaporator as the components with the most significant exergy destruction.

In total, the system produces 76 kWh of electricity, while the overall exergy loss amounts to 1696 kWh. This exergy analysis highlights the key areas of inefficiency and provides valuable insights for improving system performance. By addressing the components with the highest exergy losses, the analysis paves the way for optimizing energy conversion processes and enhancing the overall efficiency of the multi-energy production system, ultimately reducing its environmental impact.

Fig. 18 illustrates the cost rate distribution across the components of the multi-energy production system, which includes the PVT panels, ORC unit, absorption chiller, and water heater. The ORC unit incurs the highest cost rate at 1.5075 $/h, driven by the expense of its four key components: the pump, condenser, evaporator, and turbine. Moreover, the figure shows the breakdown of the ORC unit cost rate, in which the turbine has the highest cost rate with 0.8187 $/h. This reflects the ORC's complexity and highlights the need for optimization to enhance cost efficiency.

The PVT panel follows with a cost rate of 0.0107 $/h, significantly lower than that of the ORC unit, reflecting its simpler operation within the energy production process. In contrast, the absorption chiller and water heater exhibit the lowest cost rates among the system's components. This cost distribution emphasizes the varying economic contributions of each component and points to potential areas for targeted cost optimization to improve the system's overall cost-effectiveness.

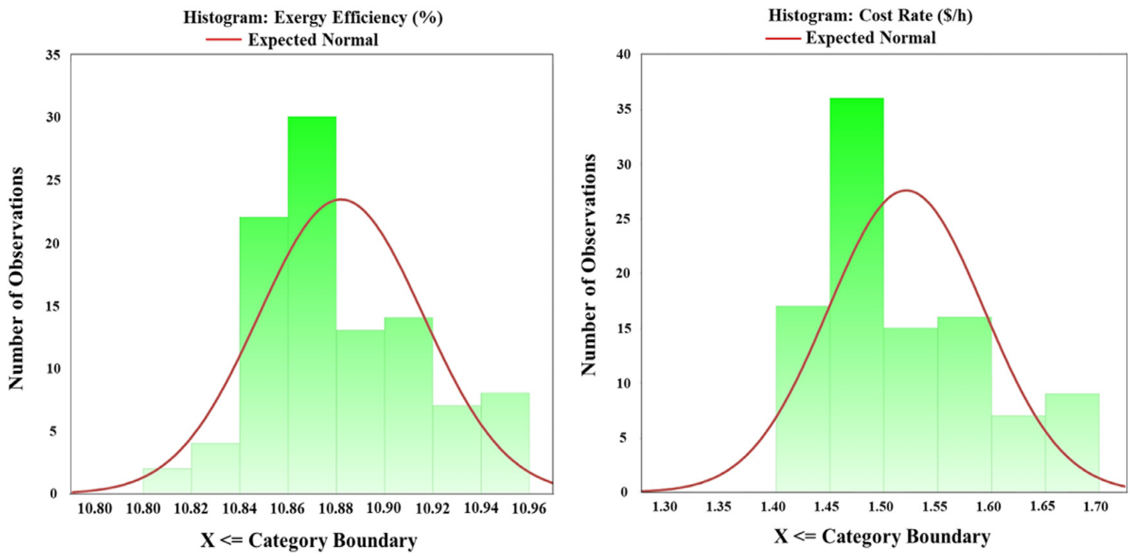

Fig. 15. Histograms of the frequency distribution of two objective functions under investigation.

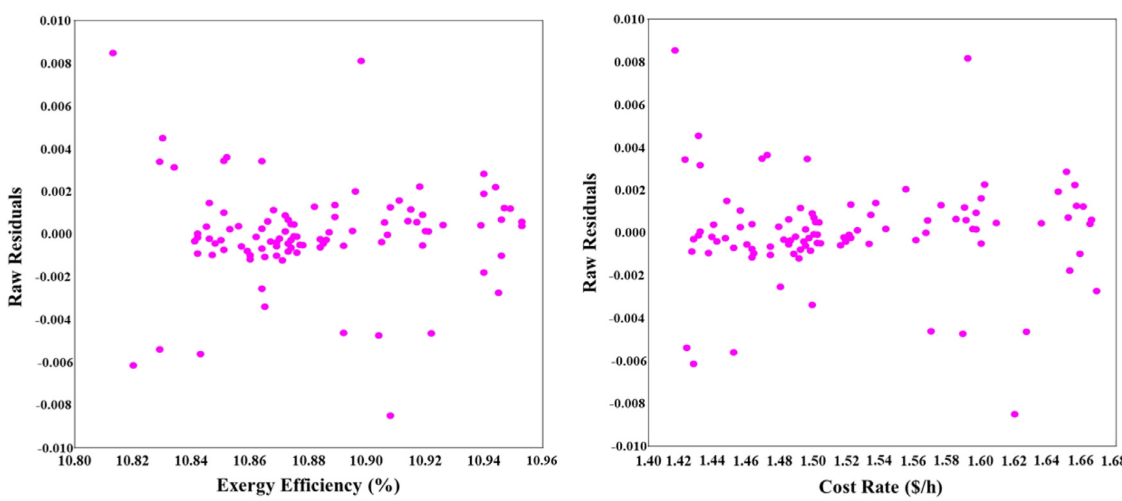

Fig. 16. Raw residual for the exergy efficiency and cost rate.

5. Case study

In this study, the impact of climate variations along the route of a passenger train traveling from southern Iran to the capital, Tehran, is thoroughly investigated. The analysis focuses on five key stations—Ahvaz, Khorramabad, Arak, Qom, and Tehran—considering the weather conditions at each station during the train's 17-hour journey. The study evaluates the performance of the train's energy production system, specifically in terms of electricity generation, heating, and cooling, to determine how varying climatic conditions across different regions influence system efficiency and output. The heating and cooling loads are calculated using energy balance equations, incorporating external temperature fluctuations, train insulation properties, and internal heat sources such as passengers, lighting, and onboard equipment. The set-point temperatures are set at 20 °C for heating and 24 °C for cooling, ensuring compliance with passenger comfort standards.

Since 2013, Fadak trains have been operating on the Iranian railway, recognized as the first five-star luxury trains in the country. These trains are designed to enhance the standards of rail travel, offering a higher level of comfort and service. Fadak train can accommodate approximately 400 passengers across wagons that include 10 compartments, each designed for a total of 40 passengers per wagon. The modern amenities provided on Fadak train, such as air conditioning, entertainment systems, and restaurant-quality catering, have set a new benchmark for premium rail travel in Iran.

Fig. 19 offers a visual representation of the train's exterior and interior design, as well as a map of the route through the selected cities, providing critical geographic and climatic context for the energy system's operation. The objective of this case study is to evaluate the integrated electricity, heating, and cooling outputs of the proposed system—alongside the current energy production system—throughout the journey, based on the specifications provided in Table 9 and using the optimal design variables identified in the previous section. The focus of the case study is to examine the feasibility of the system in terms of energy production under varying external ambient conditions. To avoid additional complexity to the proposed system, the roles and functions of thermal and electrical storage are excluded from the analysis.

Fig. 20 illustrates monthly variations in the mean monthly ambient air temperature and solar radiation intensity at five stations under study. Fig. 20(a) indicates the significant monthly variations in ambient temperature (T_0) at the passenger train stations along the route from southern Iran to Tehran. Ahvaz stands out as having the highest average temperature compared to the other cities, reflecting its geographic location in one of the hottest regions of Iran, where temperatures on some

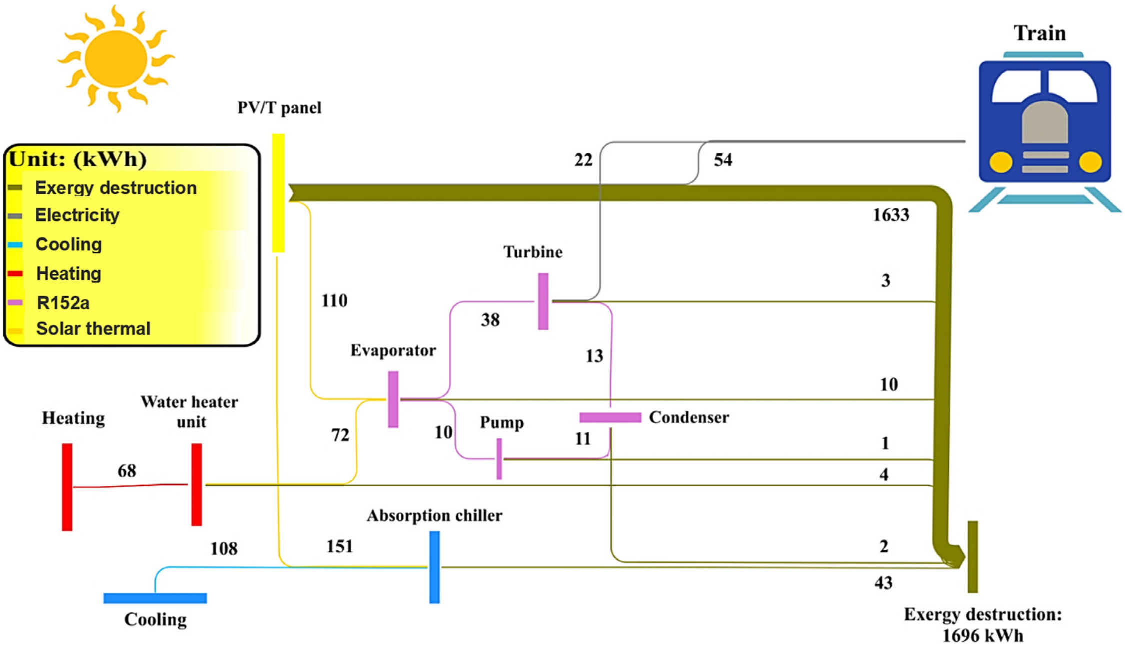

Fig. 17. Exergy analysis of the optimized multi-energy production system.

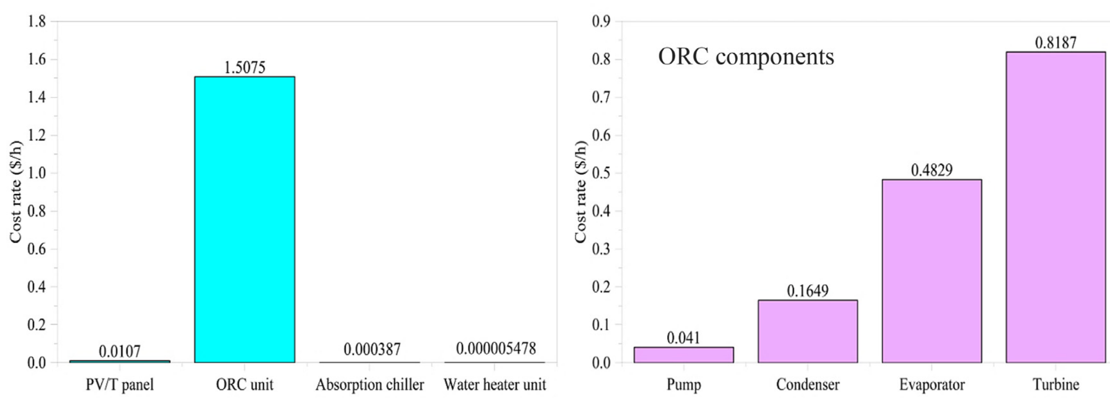

Fig. 18. Breakdown of the system cost rate.

Fig. 19. Visual representation of the passenger train and its route map.

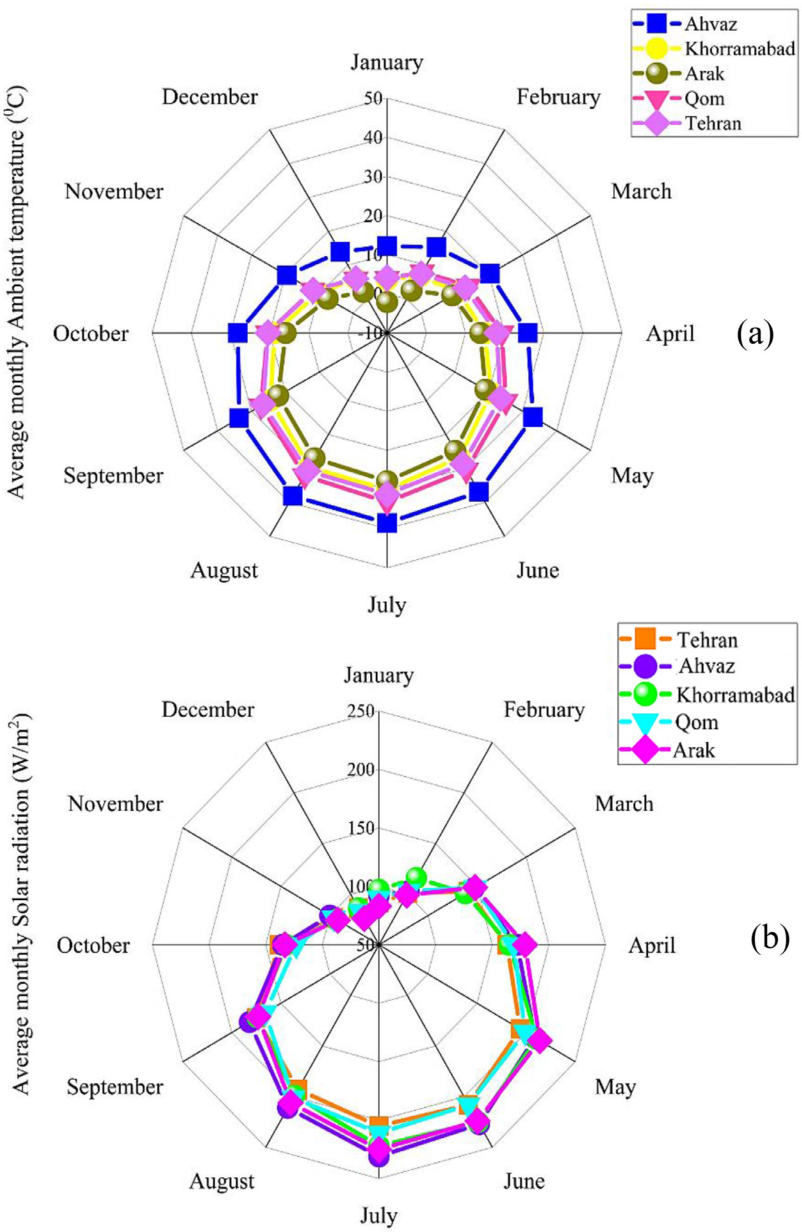

Fig. 20. Variations in the mean monthly ambient air temperature (a) and solar radiation intensity (b) at five different stations.

Table 9
Technical specifications of the passenger train considered in the case study.

Parameter	Unit	Value
Number of wagons	-	10
Roof space per wagon	m^2	72
Available space on the roof for PVT	m^2	62
Number of passengers per wagon	-	40
Set-point temperature (cooling)	°C	20 (±0.5)
Set-point temperature (heating)	°C	24 (±0.5)
Route operational time	hr	17
Number of stops	-	5
Stop duration	min	20
PVT type	-	Flat plate
PVT module size	m^2	2.21 (1.3 × 1.7)
P_{max} (total) per module	kW	1.88
Tilt angle	degree	30
Thermal efficiency	%	66.5
Electrical efficiency	%	19.0

summer days exceed 50 °C. In contrast, the cities of Arak and Khorramabad experience the lowest average temperatures, with values dropping below freezing during the colder months, largely due to their higher elevations and cooler climates. These hourly temperature fluctuations, ranging from −10 °C to over 50 °C, underscore the considerable climatic diversity encountered along the train's journey, which has a striking impact on the energy consumption and operational efficiency of the train's multi-energy production system. As Fig. 20(b) shows, solar radiation also plays a significant role in the performance of the energy system, with Ahvaz receiving the highest levels of solar intensity, reaching up to 240 W/m^2. In contrast, Tehran and Khorramabad experience the lowest mean annual solar radiation among the selected cities. These climatic variations emphasize the importance of dynamic energy system adaptation, integrating energy storage, smart control strategies, and hybrid heating-cooling technologies to maintain operational efficiency across varying climatic conditions.

To shed light on the energy consumption of the passenger train, Fig. 21 illustrates the variations in hourly energy use across different

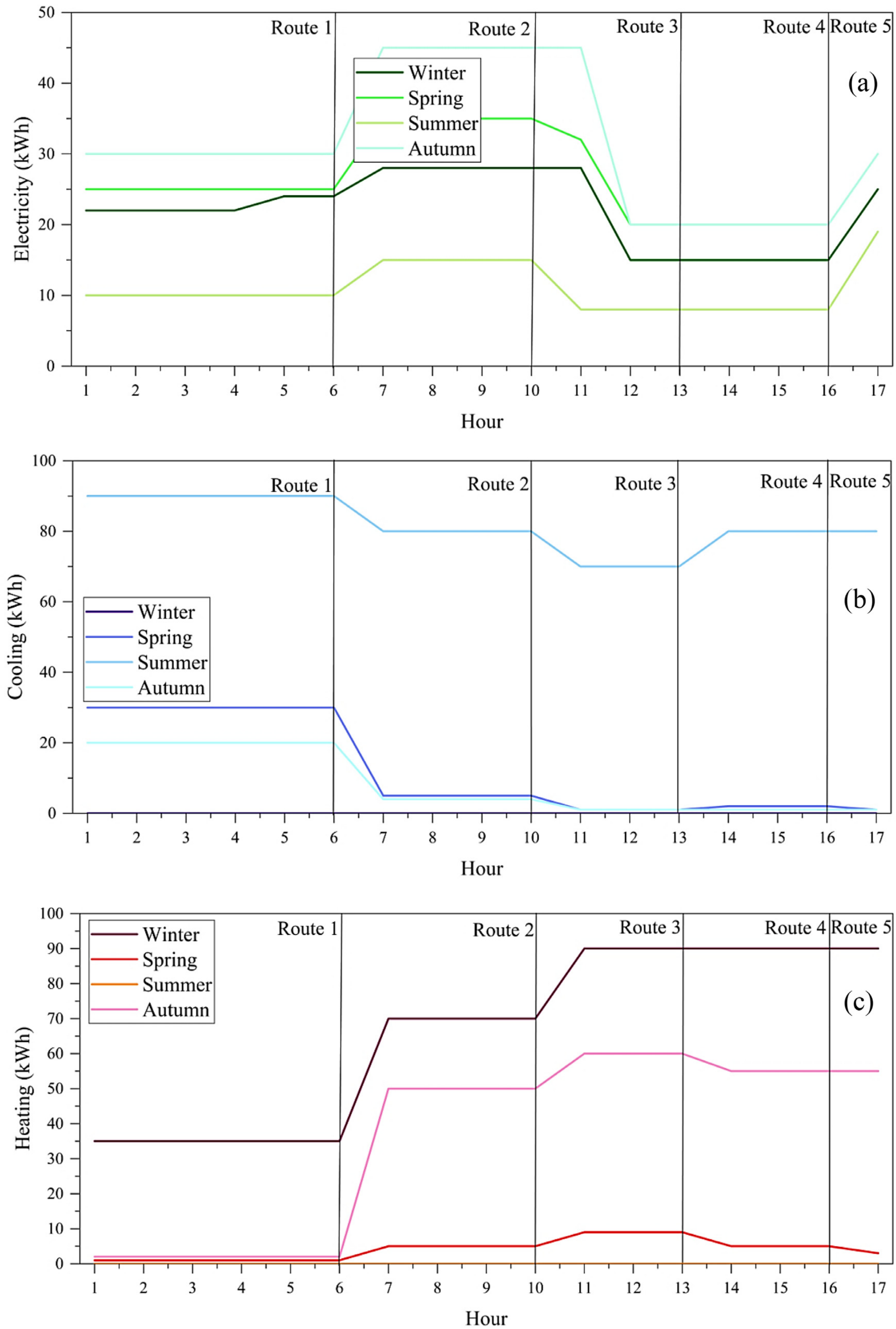

Fig. 21. The hourly energy use by the passenger train, including electricity (a), cooling (b), and heating (c).

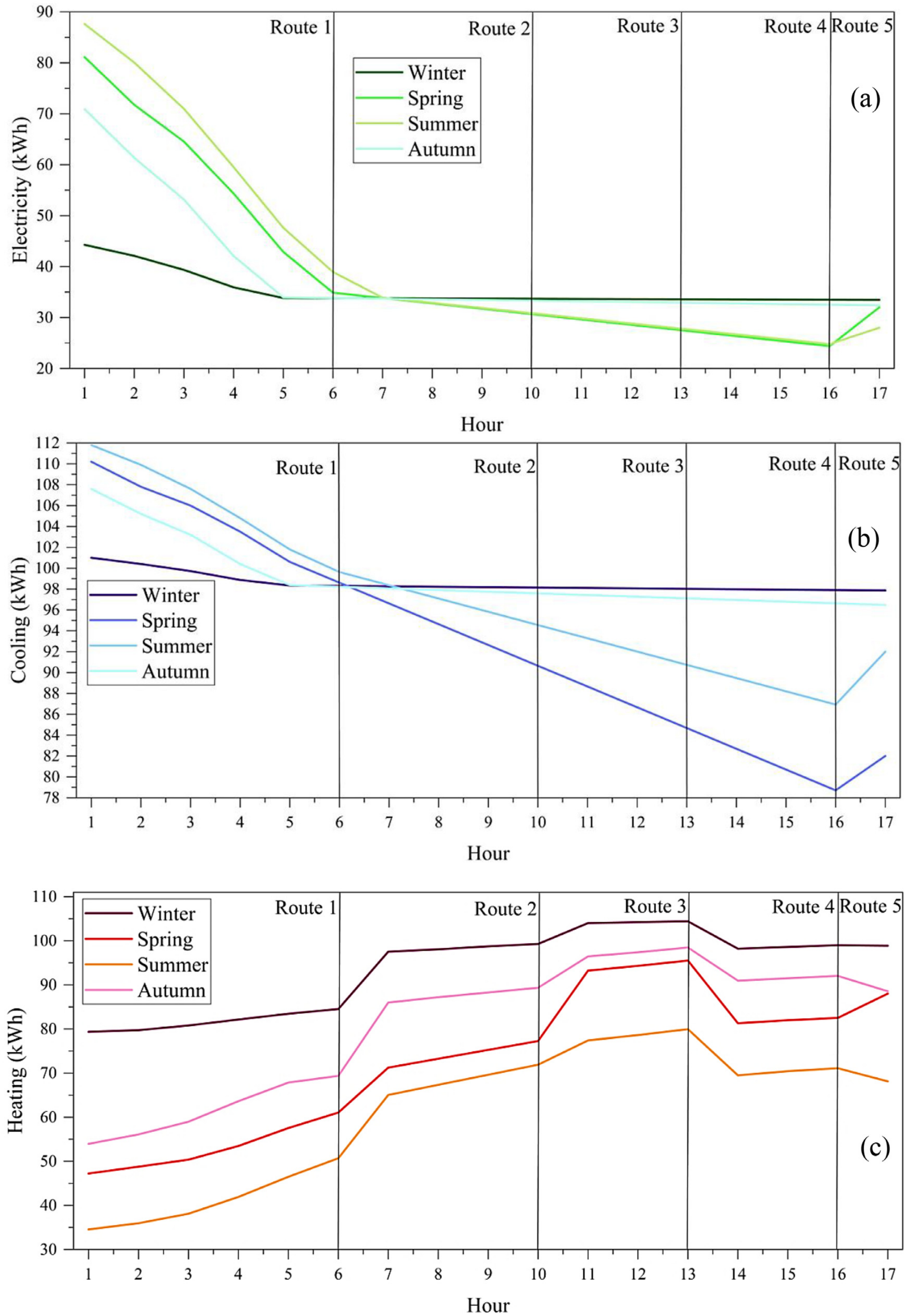

Fig. 22. Hourly net energy generation of the system: Electricity (a), cooling (b), and heating (c).

seasons. Fig. 21(a) shows that electrical energy consumption peaks between the seventh and eleventh hours of operation in all seasons, with a maximum of 45 kWh in autumn along route 2 (Ahvaz to Khorramabad). It should be noted that this energy is solely used for lighting and power outlets in the passenger compartments. The cooling and heating needs are met by the multi-energy production system, which eliminates the need for electrically powered cooling and heating devices.

Figs. 21(b) and (c) depict the cooling and heating energy consumption over the 17-hour journey. Cooling energy ranges from 0 to 90 kWh, with no demand in winter and the highest consumption during summer and spring, especially in subtropical regions like Ahvaz (route 1). Heating energy consumption, on the other hand, fluctuates between 0 and 95 kWh, peaking in winter and autumn, particularly in colder areas such as Arak and Qom (routes 3 and 4). During summer, no heating is required. These findings are crucial for optimum sizing the train's heating and cooling systems, ensuring efficient energy use while maintaining passenger comfort throughout the year.

Fig. 22 illustrates the hourly variations in net energy generation—including electricity, cooling, and heating—produced by the system as the train travels through five stations along its route across four seasons. Fig. 22(a) demonstrates a clear positive correlation between increasing solar radiation, heat input to the evaporator, and system power output, especially during the hotter hours. As solar radiation intensifies, system components such as PVT panels and the ORC turbine operate more efficiently, significantly boosting electricity generation (up to 87 kWh). This enhanced power production allows the system to meet the train's energy demands more effectively, highlighting the pivotal role solar energy plays in optimizing performance during periods of high heat and strong solar input.

Fig. 22(b) shows that as solar radiation and the inlet temperature of the absorption chiller rise, the cooling output of the system also increases. This is due to the improved absorption of thermal energy by the chiller, which is essential for maintaining passenger comfort, particularly during hot weather. A notable cross-point is observed at around 100 kWh in the sixth hour of operation for cooling production across all seasons. The figure emphasizes the critical role of solar energy in driving the absorption chiller, demonstrating how maximizing solar input and maintaining optimal inlet temperatures can significantly enhance cooling efficiency. Conversely, Fig. 22(c) depicts an inverse relationship between solar radiation, ambient temperature, and heating output. A striking difference can be observed between the heating production in winter and other seasons, which reaches 45 kWh, i.e., between winter and summer. As temperatures rise and solar radiation increases, the system reduces heating output, reflecting lower demand for heat during the warmer hours. This adaptive response ensures efficient modulation of the system's energy production, reducing unnecessary heating during summer while maintaining adequate heat supply in colder seasons.

The analysis of the system's energy supply capabilities for the passenger train demonstrates its strong potential to meet energy demands efficiently. The system not only satisfies the train's electricity, cooling, and heating requirements during most periods of operation, but also generates a considerable surplus of energy throughout the year. This surplus can be quantified by calculating the difference between the energy produced by the system and the energy consumed by the train, highlighting the potential for alternative energy utilization.

In terms of heating and cooling energy storage, the highest potential is observed along Route 3, with peak heating energy storage occurring in spring and maximum cooling energy storage in winter. To optimize the use of this surplus energy, several strategies can be implemented, including discharging excess energy at intermediate stations, utilizing it at the destination, and storing it in dedicated wagons. These approaches not only enhance the system's overall energy efficiency but also support the sustainability of the rail network by minimizing energy waste and promoting the integration of renewable sources. Through effective storage and repurposing of surplus energy, the passenger train system can serve as a flexible asset within both the transportation and energy sectors.

6. Limitations and future work

Although the proposed model offers a sustainable and cost-efficient solution for passenger train operations, some limitations must be acknowledged. The study assumes steady-state conditions, neglecting transient operational variations such as daily and seasonal fluctuations in solar radiation, variable passenger loads, and train acceleration patterns. These factors can impact energy demand and system performance, particularly for routes with intermittent solar availability. The case study was conducted under idealized solar irradiance conditions, namely a case with abundant year-round solar irradiance, which may not fully reflect energy supply challenges during cloudy weather or nighttime operations. Furthermore, to avoid adding complexity to the proposed system, the roles and functions of thermal and electrical storage are intentionally excluded from the analysis, allowing for a clearer assessment of the core production systems. Indeed, the current study primarily focuses on the performance and multi-objective optimization of the production systems, disregarding the role of energy storage systems.

Future work should address these limitations by incorporating transient simulations to account for dynamic variations in solar availability and train energy demand. To ensure a continuous and reliable power supply, a hybrid renewable energy storage system that combines high-density lithium-ion batteries with efficient thermal energy storages should be explored, enabling better management of supply-demand mismatches and enhancing overall system flexibility. Optimizing train scheduling and energy dispatch can improve efficiency by aligning energy generation with demand, and integrating smart energy management systems with real-time adaptive control can further reduce losses and enhance system resilience. Additionally, refining the cost estimation approach to account for maintenance, component degradation, and long-term economic factors will improve economic feasibility assessments. Finally, expanding the study to include different climatic zones and rail routes would improve the generalizability of the findings.

7. Conclusion

The present study aimed to design and optimize a solar-driven multi-energy production system to meet the energy demands of passenger trains. The proposed configuration incorporates PVT panels, an ORC system, an absorption chiller, and a water heater unit. System modeling was conducted using the EES software, and optimization was achieved through a multi-criteria optimization framework coupling RSM utilizing Design Expert software and ANN methods using Statistica software to enhance optimization accuracy. A case study evaluated the feasibility of implementing the proposed system on passenger trains, focusing on a real-case train in the route of Khorramshahr-Tehran (Iran), under varying weather conditions at five stations over the course of a year.

The bi-level optimization framework effectively allowed for trade-offs between conflicting design variables. Using 100 optimal points derived from the RSM and imported into the neural network method yielded an exergy efficiency of 10.88 % and a cost rate of 1.520 $/h. The economic analysis revealed that the ORC unit, solar panel, and absorption chiller unit have the highest cost rates, indicating significant investment in these components. Additionally, the exergy analysis showed that the most substantial exergy destruction occurs in the PVT panels, absorption chillers, and evaporators, highlighting areas for potential efficiency improvements.

The proposed model demonstrated promising performance by meeting the passenger train's energy demands during most periods of operation, while also producing surplus electricity, cooling, and heating that could be directed to storage. The proposed cogeneration system not only highlights the potential of solar energy in the transportation sector but also demonstrates the effectiveness of advanced modeling and optimization techniques in improving system performance and economic viability. However, further research is needed to evaluate the system under a wider range of climatic conditions and operational demands. Expanding the study to include diverse climate zones and rail routes—while addressing the aforementioned limitations—would enhance the robustness and generalizability of the findings.

Declaration of competing interest

The authors declare that they have no known competing financial interests or personal relationships that could have appeared to influence the work reported in this paper.

CRediT authorship contribution statement

Ehsanolah Assareh: Writing – original draft, Validation, Software, Methodology, Investigation, Conceptualization. **Aminhossein Jahanbin:** Writing – review & editing, Writing – original draft, Visualization, Supervision, Investigation, Formal analysis. **Nima Izadyar:** Writing – original draft, Visualization, Investigation, Formal analysis. **Mohammad Barati:** Writing – original draft, Resources, Investigation, Data curation. **Neha Agarwal:** Writing – original draft, Software, Methodology, Investigation, Formal analysis.

References

[1] "The Paris Agreement | UNFCCC." https://unfccc.int/process-and-meetings/the-paris-agreement/the-paris-agreement.
[2] A. Behzadi A, S.M. Alirahmi, H. Yu, S. Sadrizadeh, An efficient renewable hybridization based on hydrogen storage for peak demand reduction: a rule-based energy control and optimization using machine learning techniques, J. Energy Storage 57 (2023) 57106168, doi:10.1016/j.est.2022.106168.
[3] O. Ozkan, B.S. Eweade, O. Usman, Assessing the impact of resource efficiency, renewable energy R&D spending, and green technologies on environmental sustainability in Germany: evidence from a Wavelet Quantile-on-Quantile Regression, J. Clean. Prod. 450 (2024) 141992, doi:10.1016/j.jclepro.2024.141992.
[4] International Energy Agency (IEA)Net Zero by 2050, IEA, Paris, 2021 https://www.iea.org/reports/net-zero-by-2050.
[5] E. Linstad, T. Ask, P. Cariou, G.S. Eskeland, A. Rialland, Wise use of renewable energy in transport, Transp. Res. Part D 119 (2023) 103713, doi:10.1016/j.trd.2023.103713.
[6] B. Heid, M. Kässer, T. Müller, S. Pautmeier, Fast transit: why urban e-buses lead electric-vehicle growth, McKinsey Center for Future Mobility, McKinsey & Company, 2018.
[7] J. Grütter, A. Frecon, A. Ferreira, L. Gong, L. Song, J. Wang, et al., SUSTAINABLE TRANSPORT SOLUTIONS: Low-Carbon Buses in the People's Republic of China, Asian Development Bank, 2018.
[8] Transport Ma. European Clean Bus Deployment Initiative. European Commission.
[9] S. Brozan, S. Giannelos, G. Strbac, Strategic network expansion planning with electric vehicle smart charging concepts as investment options, *Adv. Appl. Energy* 5 (2022) 100077, doi:10.1016/j.adapen.2021.100077.
[10] International Energy Agency (IEA) - The Future of rail: Opportunities for energy and the environment (2019). https://www.iea.org/reports/the-future-of-rail.
[11] L. Jia, J. Ma, P. Cheng, Y. Liu, A perspective on solar energy-powered road and rail transportation in China, CSEE J. Power Energy Syst. 6 (4) (2020) 760–771, doi:10.17775/CSEEJPES.2020.02040.
[12] L. Abdolmaleki, A. Jahanbin, U. Berardi, Net-zero energy management through multi-criteria optimizations of a hybrid solar-hydrogen energy system for a laboratory in Toronto, Canada, Energy Build. 312 (2024) 114186, doi:10.1016/j.enbuild.2024.114186.
[13] X. Huang, F. Li, L. Lu, Z. Li, X. Yang, J. Yan, Depth optimization of solidification properties of a latent heat energy storage unit under constant rotation mechanism, Energy Build. 290 (2023) 113099, doi:10.1016/j.enbuild.2023.113099.
[14] E. Assareh, M. Parvaz, S. Hoseinzadeh, M. Lee, A new analysis for a concentrated solar power-based cogeneration system with molten salt energy storage and heat recovery steam generator – case study – (USA, France, Canada), Renewable Energy Focus 46 (2023) 256–280, doi:10.1016/j.ref.2023.06.008.
[15] A. Jahanbin, U. Berardi, Interplay between renewable energy factor and levelized costs in PV-driven buildings using hydrogen fuel cell system as an energy storage solution, Int. J. Hydrogen Energy 122 (2025) 22–34, doi:10.1016/j.ijhydene.2025.03.263.
[16] Y. Khan, R.S. Mishra, Performance analysis of solar driven combined recompression main compressor intercooling supercritical CO_2 cycle and organic Rankine cycle using low GWP fluids, Energy Built Environ. 3 (4) (2022) 496–507, doi:10.1016/j.enbenv.2021.05.004.
[17] M.E. Zayed, M.M. Aboelmaaref, M. Chazy, Design of solar air conditioning system integrated with photovoltaic panels and thermoelectric coolers: experimental analysis and machine learning modeling by random vector functional link coupled with white whale optimization, Thermal Sci. Eng. Progr. 44 (2023) 102051, doi:10.1016/j.tsep.2023.102051.
[18] D. Lopez-Pascual, I. Valiente-Blanco, O. Manzano-Narro, M. Fernandez-Munoz, E. Diez-Jimenez, Experimental characterization of a geothermal cooling system for enhancement of the efficiency of solar photovoltaic panels, Energy Reports 8 (15) (2022) 756–763, doi:10.1016/j.egyr.2022.10.154.
[19] L. Abdolmaleki, A. Jahanbin, U. Berardi, Towards standalone commercial buildings in the Mediterranean climate using a hybrid metal hydride and battery energy storage system, J. Build. Eng. 96 (2024) 110567, doi:10.1016/j.jobe.2024.110567.
[20] F. Esmaeilion, M. Zarnoush, A.H. Azad, H. Jafarizadeh, et al., Comparative investigation for sustainable freshwater production in hybrid multigrid systems based on solar energy, J. Clean. Prod. 476 (2024) 143694, doi:10.1016/j.jclepro.2024.143694.
[21] Y. Wang, Y. Fan, D. Wang, Y. Liu, Z. Qiu, J. Lie, Optimization of the areas of solar collectors and photovoltaic panels in liquid desiccant air-conditioning systems using solar energy in isolated low-latitude islands, Energy 198 (2020) 117324, doi:10.1016/j.energy.2020.117324.
[22] R. Senthil, A technical note on integrating thermal energy systems into solar photovoltaic panels toward a circular economy, Renewable Energy Focus 42 (2022) 97–100, doi:10.1016/j.ref.2022.06.002.
[23] M. Bartłomiejczyk, Potential application of solar energy systems for electrified urban transportation systems, Energies (Basel) 11 (4) (2018) 954, doi:10.3390/en11040954.
[24] H. Chen, Y. Sui, W.-L. Shang, R. Sun, et al., Towards renewable public transport: mining the performance of electric buses using solar-radiation as an auxiliary power source, Appl. Energy 3215 (2022) 119863, doi:10.1016/j.apenergy.2022.119863.
[25] P. Ahmadi, I. Dincer, M.A. Rosen, Exergy, exergoeconomic and environmental analyses and evolutionary algorithm based multi-objective optimization of combined cycle power plants, Energy 36 (10) (2011) 5886–5898, doi:10.1016/j.energy.2011.08.034.
[26] Multi-criteria design optimization and thermodynamic analysis of a novel multi-generation energy system for hydrogen, cooling, heating, power, and freshwater. Int, J. Hydrogen Energy 45 (30) (2020) 15047–15062, doi:10.1016/j.ijhydene.2020.03.235.
[27] A.R. Razmi, M. Janbaz, Exergoeconomic assessment with reliability consideration of a green cogeneration system based on compressed air energy storage (CAES), Energy Convers. Manage 204 (2020) 112320, doi:10.1016/j.enconman.2019.112320.
[28] R. Ghelich, M.R. Jahannama, H. Abdizadeh, F.S. Torknik, M.R. Vaezi, Central composite design (CCD)-Response surface methodology (RSM) of effective electrospinning parameters on PVP-B-Hf hybrid nanofibrous composites for synthesis of HfB2-based composite nanofibers, Composites Part B 166 (2019) 527–541, doi:10.1016/J.COMPOSITESB.2019.01.094.
[29] K. Zhoo, J. Mao, Y. Li, H. Zhang, Z. Deng, Prediction and parametric analysis of 3D borehole and total internal thermal resistance of single U-tube borehole heat exchanger for ground source heat pumps, Energy Built Environ. 4 (2) (2023) 179–194, doi:10.1016/j.enbenv.2021.11.001.
[30] D.L. Allaix, V.I. Carbone, An improvement of the response surface method, Struct. Safety 33 (2) (2011) 165–172, doi:10.1016/j.strusafe.2011.02.001.
[31] B. Chetia, S. Debbarma, F. Ahmed, Parametric optimization of variable compression ratio diesel engine run on waste cooking biodiesel with CeO2 nanoparticles using response surface methodology (RSM) technique, Fuel 389 (2025) 134544, doi:10.1016/j.fuel.2025.134544.
[32] A. Jahanbin, L. Abdolmaleki, U. Berardi, Cross-climate analysis of techno-economic metrics in bi-level electrical and hydrogen storage systems for off-grid electrification of buildings, J. Energy Storage 107 (2025) 114938, doi:10.1016/j.est.2024.114938.
[33] A. Sarlak Roshani, E. Assareh, A. Ershadi, M. Carvalho, Optimization of a hybrid renewable energy system for off-grid residential communities using numerical simulation, response surface methodology, and life cycle assessment, Renew. Energy 236 (2024) 121425, doi:10.1016/j.renene.2024.121425.
[34] M.S. Alam, J.B. Deb, A. Al Amin, S. Chowdhury, An artificial neural network for predicting air traffic demand based on socio-economic parameters, Decis. Analytics J. 10 (2024) 100382, doi:10.1016/j.dajour.2023.100382.
[35] S. Abut, H. Okut, K.J. Kallail, Paradigm shift from Artificial Neural Networks (ANNs) to deep Convolutional Neural Networks (DCNNs) in the field of medical image processing, Expert Syst. Appl. 244 (2023) 122983, doi:10.1016/j.eswa.2023.122983.
[36] E. Bas, E. Egrioglu, T. Cansu, Robust training of median dendritic artificial neural networks for time series forecasting, Expert Syst. Appl. 238 (2024) 122080, doi:10.1016/j.eswa.2023.122080.
[37] E. Amiri Rad, S. Mohammadi, E. Tayyeban, Simultaneous optimization of working fluid and boiler pressure in an ORC for different heat source temperatures, Energy 194 (2019) 116856, doi:10.1016/j.energy.2019.116856.